A disordered lamellar structure in the isotropic phase of a ternary double-chain surfactant system

Ian S. Barnes, Paul-Joël Derian, Stephen T. Hyde, Barry W. Ninham, Thomas Zemb

Classification
Physics Abstracts
61.10L — 61.12E — 64.70M — 66.10E

A disordered lamellar structure in the isotropic phase of a ternary double-chain surfactant system

Ian S. Barnes ([1, 2, *]), Paul-Joël Derian ([2]), Stephen T. Hyde ([1]), Barry W. Ninham ([1]) and Thomas N. Zemb ([1, 2])

([1]) Department of Applied Mathematics, Australian National University, Canberra ACT 2601, Australia
([2]) Département des Lasers et de Physico-Chimie, C.E.A. Saclay, F-91191 Gif-sur-Yvette, France

(*Received 13 December 1989, revised 10 July 1990, accepted 13 July 1990*)

Résumé. — La phase fluide isotrope « anormale » du système DDAB/tétradécane/eau est très différente des autres microémulsions dans des systèmes voisins. A partir des mesures de diffusion de rayons-X et de neutrons à l'échelle absolue nous montrons que la structure est celle d'une bicouche froissée aléatoire contenant de l'eau. Les autres structures en lamelles aléatoirement connectées décrites jusqu'à présent sont restreintes à un domaine étroit de composition et de température. Dans le système décrit ici, la rigidité intrinsèque de la bicouche et sa courbure faible permettent la formation de cette structure dans une grande région du diagramme de phases ternaire à température ambiante. Les autres modèles structuraux de microémulsions sont discutés et leurs prédictions confrontées aux résultats expérimentaux.

Abstract. — The « anomalous » fluid isotropic phase in the DDAB/tetradecane/water system differs in important ways from microemulsion phases in related systems, and is thus a useful test for models. On the basis of absolute scaled neutron and X-ray scattering data we show here that the microstructure is best characterised as a randomly folded reverse bilayer. All previously reported examples of this structure are restricted to a narrow range of composition and temperature. In this case of a stiff bilayer with low spontaneous interfacial curvature it extends over a large region of the ternary phase diagram at room temperature, the boundaries of which are explained in terms of simple geometric constraints. Other possible microstructures are critically reviewed.

1. Introduction.

Ternary systems containing the double-chain surfactant didodecyldimethylammonium bromide (DDAB) form microemulsions over a large composition range. We have previously explained the behaviour of these fluid, isotropic solutions by adopting a geometric approach [1-5] : the constraints on microstructure are that the polar volume fraction Φ, the interfacial area per unit volume Σ and the interfacial curvature (set by the surfactant packing parameter $v/a\ell$ [6]) must match the values set by the composition. We have constructed an approximate

(*) *Present address :* CRPP/CNRS Château Brivazac, Avenue Schweitzer, F-33600 Pessac, France.

model which satisfies these constraints using spheres and cylinders decorating a random Voronoï lattice (the DOC cylinders model). For the systems with DDAB, water and alkanes from cyclohexane to dodecane, this allows prediction of approximate phase boundaries [7] and conductivity thresholds [4] and calculation of full scattering spectra on absolute scale [8] for all these systems. Other microemulsion models either introduce free parameters or are incompatible with the experimental data [9].

The system DDAB/tetradecane/water exhibits qualitatively different behaviour to ternary systems containing the same surfactant but shorter-chain alkanes and alkenes [10-13]. The phase diagram has been studied in detail by Larché [14] from whose work figure 1 is redrawn. At room temperature there is a large isotropic phase in the centre of the three-phase triangle, which we refer to as L_x. This solution does not show Bragg peaks and hence must have a disordered structure.

Unlike the L_2 phases for the shorter oils, the L_x phase cannot be diluted with tetradecane without separating into two phases. On dilution with water it separates into two phases with the water-rich lamellar phase L_α^1 in excess, rather than demixing to spill out water, which is the usual behaviour of such systems [15]. Towards the top of the phase diagram, the L_x phase is in equilibrium with excess oil, whereas increase in surfactant concentration gives rise to equilibrium with the surfactant-rich lamellar phase L_α^2.

If one dilutes the L_x phase with a binary surfactant/water mixture at constant surfactant to water ratio, a cubic phase is obtained. This transition is extremely temperature-sensitive [14].

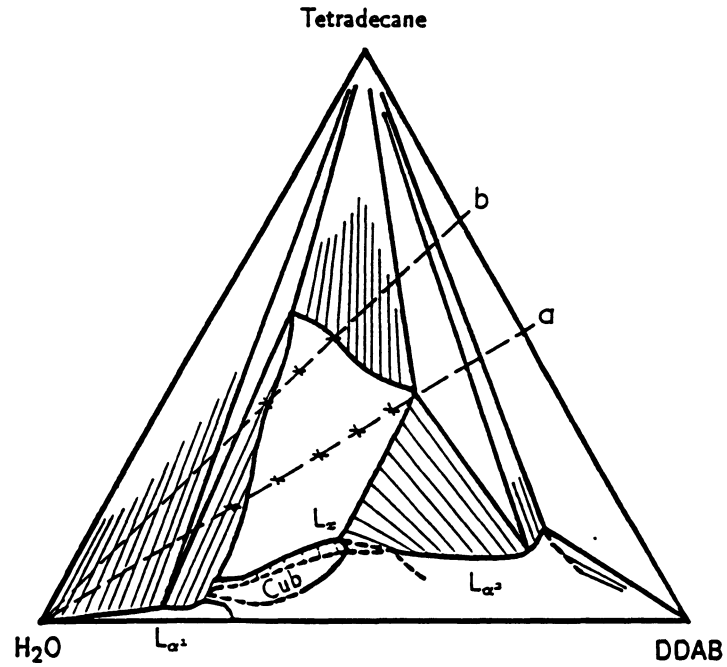

Fig. 1. — Phase Diagram of the DDAB/tetradecane/water system, redrawn from Larché [14]. The label L_x refers to the microemulsion phase of interest, L_α^1 to the water-rich lamellar phase, L_α^2 to the surfactant-rich lamellar phase, and Cub to the cubic phase. The lines marked a and b refer to the water dilution lines studied ; along each the samples are numbered in order of increasing water content. Compositions are given in table I. Slight discrepancies between the marked sample positions and the phase boundaries are the result of the different temperatures used. The tie lines drawn are illustrative only.

As for the other oils, the cubic phase region is probably a reversed bilayer (water inside the film separating two bulk oil regions) lying on a periodic minimal surface with a cubic underlying lattice [16]. For the other oils, this region contains several structures with different topologies [17, 18].

In contrast to the systems with short chain alkanes or alkenes [10-13], the conductivity of the L_x phase is always high, which means that the structure has to be water continuous throughout. There is no antipercolation. If oil penetration determines interfacial curvature [13], then the surfactant parameter $v/a\ell$ is expected to be close to one since tetradecane does not penetrate the surfactant tails. It is reasonable to expect a value between 0.95 and 1.05.

These observations suggest a qualitatively different picture to that established for the systems with shorter-chain oils. As the tetradecane does not interpenetrate the surfactant tails, the interface is consequently much flatter. This conclusion is supported by the observation that upon addition of strongly penetrating hexane, the tetradecane system reverts to the previous behaviour, with both a percolation threshold and the possibility of dilution to the oil corner. Addition of a single-chain surfactant has the same effect, while adding a long-chain alcohol to the dodecane system switches its behaviour to that of tetradecane. All of this can be explained by a qualitative difference in behaviour between systems with $v/a\ell \approx 1$ and $v/a\ell \gg 1$.

Since there is no cosurfactant added and essentially no oil penetration, we cannot be satisfied by a model which requires *ad hoc* variation of the total interface per unit volume Σ or the packing parameter $v/a\ell$ with composition. Without the fixed area constraint one could fit all scattering curves, even on absolute scale, to a model of ellipsoids or polydisperse spheres [9]. As for the other systems, the relative lack of temperature dependence of the phase diagram and of the scattering — in this case, repeat scattering runs at 80 °C show little difference in the results — suggests that the interface is rather stiff.

At first sight, no satisfactory explanation for the behaviour of this phase exists. It cannot be a dispersion of spherical droplets : water droplets in oil would not conduct and could be diluted to the oil corner ; oil droplets in water could be diluted with water. Further, neither would give reasonable curvature. It also seems unlikely to be a DOC-cylinder structure like that used to model the microemulsion phases for the shorter-chain oils, because this structure can be diluted by oil, has a high interfacial curvature and displays a conductivity percolation. A DOC-lamellar or random bilayer structure, already proposed for other ternary systems [2], is not expected to exist over a large composition range ; it is usually found in ternary or quaternary systems only over a very narrow temperature and composition range close to a lamellar phase [19, 20].

The structure of the remainder of this article is as follows. First we review the main microemulsion models found in the literature ; then present the results of our experiments ; and finally compare the predictions of the models with our data.

2. Microemulsion models.

2.1 INTERACTING SPHERICAL DROPLETS. — One supposes that one of the two volumes — polar or nonpolar — is « internal » and is distributed in a dispersion of interacting monodisperse spherical droplets. The interface Σ and the internal volume fraction Φ are set by the composition, and hence as

$$\begin{aligned} \Phi &= \frac{4}{3}\pi R^3 n \\ \Sigma &= 4\pi R^2 n , \end{aligned} \tag{1}$$

the radius R and density n of the droplets are known *a priori* at any composition.

The scattered intensity $I(q)$ can therefore be calculated on absolute scale, without any parameter, by using the factorisation [21]

$$I(q) = P(q)\, S(q) \tag{2}$$

where the form factor $P(q)$ reflects the scattering of one sphere and the structure factor $S(q)$ the interference between adjacent particles. Hayter and Penfold [21] showed that the structure factor can be calculated analytically for identical spherical particles interacting *via* a screened electrostatic potential using only three physical parameters : the effective charge per micelle, the aggregation number and the hydration. This has been extended to various types of attractive interactions using the work of Sharma and Sharma [22].

This model has been extremely useful in the exploration of micellar structure and interactions in many surfactant systems [23]. In many situations, however, the assumption of spherical droplets with predetermined radius R fails to predict the observed scattering [1, 24]. In this situation, there is a strong temptation to fit the data to another droplet radius or to allow polydisperse or elliptical aggregates, as this always allows reconciliation of the observed scattering peak with a simple structural picture [25]. This will not do, because then Σ is incompatible with the composition or the measured Porod limit. In other systems the droplet model is also incompatible with the electrical properties [9, 26] and the isoviscosity lines of the phase diagram [27]. A review of inconsistencies obtained from the droplet model is available [28].

2.2 PARAMETRIC MODELS. — A totally different approach to microemulsions is embodied in the parametric models. On the basis of general thermodynamic arguments, Teubner and Strey [29] deduce that the scattered intensity should have the form

$$I(q) = \frac{(8\,\pi/\xi)\,\bar{\eta}^2\, c_2}{a_2 + c_1\, q^2 + c_2\, q^4} \tag{3}$$

where a_2, c_1 and c_2 are parameters with $c_1 < 0$, a_2, $c_2 > 0$. This expression has been extremely successful at fitting a large number of scattering curves even on absolute scale. From the damped periodic correlation function which gives this scattering, one can then derive values for the « spatial periodicity » d, the correlation distance ξ and the internal surface Σ.

This expression has been recast by Chen *et al.* [30] in terms of a different set of parameters :

C_1, the ratio of the peak positions predicted by the Cubic Random Cell model (see below) and measured in the experiment ;
C_2, an analogue of osmotic compressibility extended to more general networks, and
C_3, which is related to interfacial behaviour and is seen at the high-q limit.

An interesting phenomenological observation made using this model is that when the peak width is large and there is strong scattering at high q, then C_3 exceeds 10. It is asserted that this is a condition for bicontinuity which is independent of such measurements as conductivity or self-diffusion [30].

Another general expression, similar to that of Teubner and Strey, has been derived by Vonk, Billman and Kaler [31]. For an ideal lamellar structure with periodicity D, water fraction ϕ and thickness polydispersity σ, they derive the correlation function $\gamma^0(r)$. They then introduce distortions — arising from twisting or bending of the lamellar structure — which cause the correlation function to decay as

$$\gamma(r) = \gamma^0(r)\, e^{-2r/d} \tag{4}$$

where d is the « distortion length ». This gives a very similar expression for the scattering to that of Teubner and Strey.

However there is no guarantee that a given set of d, ξ and Σ or of D, d and σ leads to a geometrically possible microstructure, nor do these models include any treatment of spontaneous curvature. Furthermore, both expressions depend on three parameters and hence will fit virtually any scattering curve [9].

2.3 THE RANDOM WAVE MODEL. — This model was proposed by Berk [32] using an algorithm of Cahn [33]. The idea is to produce a random structure of typical size D^* by superposing waves of wavelength D^* with random phases and directions. Space is then divided into polar and nonpolar regions by cutting the resulting random field at some chosen threshold value — the polar region is that in which the total amplitude exceeds the threshold. The threshold value is set by volume fraction.

This random structure produces a scattering peak in the desired position but it is sharp rather than broad. To rectify this, a polydispersity in the magnitudes of the wavevectors needs to be introduced. This has been done in two dimensions by Welberry [34] and in three dimensions by Berk and by Chen *et al.* [30].

With a suitable choice for the functional form of the wavelength polydispersity, this allows control over the total interface Σ and the morphology of the structure, but in a rather non-intuitive way. A better solution [35] is to remove the long-range order implied by the infinite propagation of the waves, and to introduce local correlations which allow the interfacial area and the curvature to be controlled.

2.4 THE TALMON-PRAGER MODEL. — This was the first model to offer a continuous transformation from water droplets to oil droplets *via* a bicontinuous network [36]. It is constructed as follows :

1. choose a random distribution of points in space with density n and construct a Voronoï tessellation of space using the bisector planes. The Voronoï cell belonging to each of these centres is thus the region of space which is closer to that centre than any other ;

2. fill the Voronoï cells with water or oil at random in the proportions Φ and $1 - \Phi$; Φ is thus both the number fraction of water-filled cells and the water volume fraction ;

3. place a surfactant monolayer between adjacent cells with different contents.

This structure is bicontinuous for polar volume fractions between 18 % and 82 % with a percolation threshold at 18 %. Observed electrical conductivity behaviour is often much more complicated than this. The scattering from the Talmon-Prager model has been calculated analytically [37] and has no peak, making this model incompatible with most microemulsions.

At this point it is useful to introduce formally the Talmon-Prager Repulsive (TPR) model. This is constructed as for the original Talmon-Prager model except that the initial distribution of points is subject to a condition of closest approach, thus replacing the original random distribution by a « hard sphere » distribution. This has the effect of introducing a characteristic distance in the structure and hence a peak in the scattering at $D^* \approx n^{-1/3}$.

This structure is drawn schematically in figure 2 ; it is the simplest of the models derived from a « hard core » Voronoï lattice. It is bicontinuous over some volume fraction range and is roughly equivalent to the CRC model explained below.

The simplest prediction of the TPR model is that the correlation length ℓ_c should be equal to the periodicity D^*. Such behaviour has never yet been found experimentally [38, 39]. When ℓ_c is much smaller than D^*, a local microstructure within the cells must exist, reducing ℓ_c while keeping D^* constant. Alternatively anti-correlations between the filling of adjacent

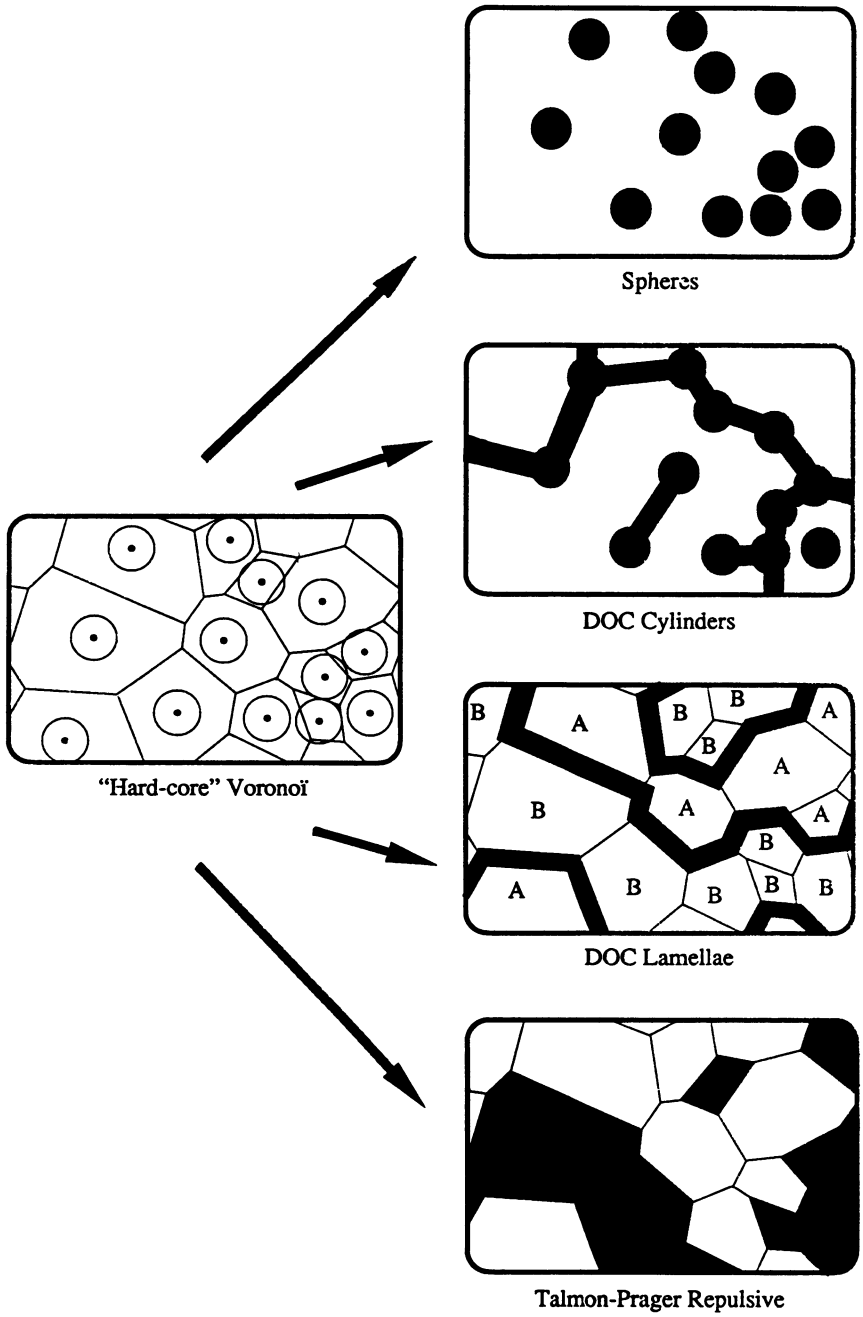

Fig. 2. — Schematic two-dimensional illustration of the different model structures derived from the hard core Voronoï lattice by the addition of microstructure. The distribution of centres of imaginary hard spheres allows the construction of a Voronoï tesselation of space. This random lattice is then used as the base on which are placed spheres, a connected network of spheres and cylinders (the DOC cylinders model) or of bilayers (the DOC lamellar model). Filling the cells at random with water or oil gives the Talmon-Prager repulsive model. Since the underlying lattice is the same for all four models, the peak position is approximately the same.

cells must be introduced, moving the scattering peak while keeping ℓ_c constant. It is possible using this latter approach (with the CRC model) to explain both the phase diagram and the peak position [40, 41].

2.5 THE CUBIC RANDOM CELL MODEL. — This model was first introduced by De Gennes as a modified Talmon-Prager model [42], and the two are clearly closely related. The construction is exactly that of the Talmon-Prager model but with the Voronoï lattice replaced by a simple cubic lattice of repeat distance ξ. Again the cells are filled with water or oil at random according to the volume fraction Φ. The edge length ξ is fixed in the random-filling approximation by

$$\xi = \frac{6\,\Phi(1-\Phi)}{\Sigma} \tag{5}$$

and the peak position will be at $D^* = 2\,\pi/q_{max} = \xi$. This model has only one distance built in. It is bicontinuous over roughly the same volume fraction as the TPR model and produces identical conductivity variation with water content.

Calculation shows that this model gives no peak at all in scattering [5, 8] : the zero of the form factor of the cubes exactly cancels the sharp Bragg peak due to the underlying lattice. This is an artefact of the exact calculation and of the random filling approximation. The peak will reappear when even slight correlations between neighbouring cells are introduced.

As noted by Auvray *et al.* [43], the peak in scattering from microemulsions is usually observed at about $D^* = 2\,\xi$, twice the distance predicted by the model. This is indeed the prediction of Milner *et al.* [44] when local anti-correlations between the filling of neighbouring cells are introduced. It is worth noting that this result is not automatic : longer-range correlations could easily produce still different peak positions.

2.6 THE DOC CYLINDERS MODEL. — Starting from the same hard core Voronoï construction as for the TPR model, we add local structure so that the model depends on two distances. These are essentially the spontaneous curvature of the interface, determined by the nature of the surfactant film, and the characteristic distance or average lattice spacing, which is determined by the composition.

The three fundamental geometric constraints on structure have to be satisfied [4].

(i) The polar volume fraction Φ is set by the composition.

(ii) The water/oil interfacial area per unit volume Σ is set by the surfactant concentration.

(iii) The average interfacial curvature must agree with the spontaneous curvature of the surfactant film as set by the surfactant parameter $v/a\ell$ (see Appendix 2).

Within the hard-core Voronoï tesselation, we construct a random connected surface with variable connectivity by gluing together spheres and cylinders. This gives an approximation, at the resolution of the scattering experiment, to the actual microstructure, which we imagine as a surface of constant $v/a\ell$ separating water and oil domains. Depending on the composition, the three constraints are satisfied by structures ranging from a dispersion of spherical droplets to highly connected networks of cylinders. The actual construction together with the predictions of peak position, approximate phase boundaries and scattering curves have been described elsewhere [4, 7, 8].

This model applies when the spontaneous radius of curvature of the surfactant film — related to persistence length and manifested here as the sphere radius R_s — is small compared to the spatial periodicity D^*. For persistence lengths of the same order of magnitude as the periodicity, that is for flatter interfaces, the behaviour goes over to that of the DOC lamellar model set out below. For more flexible films, thermal fluctuations dominate [40] and this framework will break down.

2.7 THE DOC LAMELLAR MODEL. — When $v/a\ell$ is close to one, the DOC cylinders model gives way to a random lamellar structure. This is identical to the Talmon-Prager repulsive model except that instead of water and oil separated by a monolayer, we have two fictitious different types of water separated by a normal bilayer or two types of oil separated by a reversed bilayer [2]. This structure is clearly closely related to the sponge phase model of Cates *et al.* [19] with the cubic lattice replaced by the hard sphere Voronoï. The structure is constructed as follows.

1. Take the same « hard core » Voronoï lattice as for the TPR or DOC cylinder models.
2. Label the cells A or B at random, with probabilities (and thus volume fractions) ψ and $1 - \psi$.
3. When two adjacent polyhedra have different labels, set a bilayer on the polygon between the two polyhedra. For the direct model this is a normal oil-swollen bilayer of thickness $2\ell + 2t$ separating water A from water B ; for the reversed model it is a reversed bilayer with water thickness $2t$ separating oil A from oil B.

Schematic drawings of the different microstructures derived from the Voronoï lattice are shown in figure 2 ; the local geometries of monolayers and direct and reversed bilayers are shown in figure 9. When ψ is close to $\frac{1}{2}$ the film is connected throughout space, as are the two bulk regions A and B ; when ψ is close to 0 or 1 the structure is essentially that of single-walled vesicles (Fig. 3).

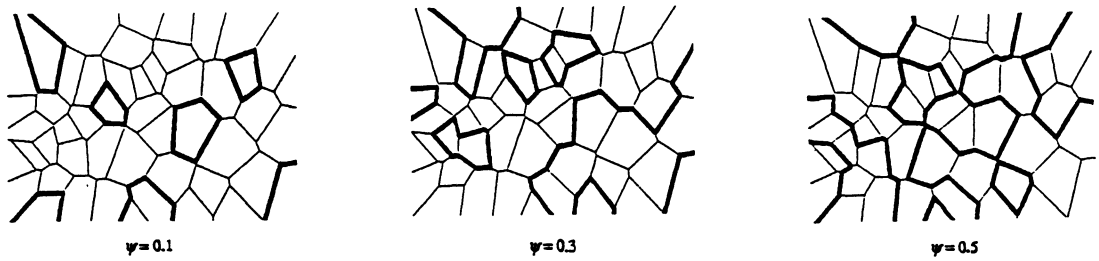

Fig. 3. — Two-dimensional illustration of the evolution of the DOC lamellar structure with increasing values of the pseudo-volume fraction ψ. When ψ is small the structure consists of isolated vesicles, while for $\psi \approx \frac{1}{2}$ it is a random connected bilayer. Note that while two-dimensional structures can never be bicontinuous, in three dimensions the film and both bulks are continuous over a large range of values of ψ.

Derivation of the area-averaged mean and Gaussian curvatures $\langle H \rangle$ and $\langle K \rangle$, and of the packing parameter $v/a\ell$ as a function of the pseudo-volume ψ are given in Appendices 2 and 3. Since the bilayer thickness can be of the same order as D^*, the average curvature at the oil-water interface is by no means negligible ; moreover, at given polar volume fraction Φ, interfacial area Σ and surfactant parameter $v/a\ell$, only one combination of half-thickness t, density of Poisson points n and pseudo-volume fraction ψ will satisfy these three constraints (Appendix 4). Assuming a DOC-lamellar structure therefore allows prediction of the approximate peak position assuming

$$D^* \approx (1.22)\, n^{-1/3} \tag{6}$$

or better, the calculation of the whole scattering curve.

2.8 « BICONTINUOUS » MODELS. — These models derive from a proposition originally made by Scriven [45] and revived more recently [46, 16]. The idea is to « melt » or disorder the structures of cubic liquid crystal phases to obtain a structure with the same properties but which does not give Bragg peaks in the scattering. Cubic phase structures have been shown in several cases to consist of a normal or reversed bilayer centered on (and presumably fluctuating about) a periodic minimal (zero mean curvature) surface which separates two distinct external subvolumes [16] ; when « melted » this is believed to give rise to the structure of the isotropic « sponge » or L_3 phase [20].

This model envisages the microstructure as that of a random bilayer, and is thus rather close to the DOC lamellar model, remembering that the latter is to be thought of as an approximation to the true structure at experimental resolution. The difference is that for the molten cubic phase the area-averaged mean curvature $\langle H \rangle$ is always zero, independently of the volume fractions on either side, while for the DOC lamellar model $\langle H \rangle$ depends on the pseudo-volume fraction ψ and is only zero when $\psi = \frac{1}{2}$ (see Appendix 3). Such considerations must depend on the treatment of the bending energy and in particular on the importance or otherwise of higher-order terms than those in the familiar Helfrich form [47].

Unfortunately, there is no known algorithm for generating a zero or other constant mean curvature surface on a random network. So this model is a qualitative one which cannot yet be tested by experiment.

3. Experimental procedure and results.

Compositions of the samples are indicated in table I, and also on the phase diagram in figure 1. Measurements were made at 28 °C ; at that temperature the samples were all monophasic. Since the molecular volumes are known, the polar volume fraction Φ can be calculated from the composition by adding the volumes of water and ionic headgroups. Since no cosurfactant is used, a good estimate of the interfacial area per unit volume Σ can be made, assuming only that the area per molecule is the same as in the neighbouring lamellar phases.

Small angle X-ray scattering experiments were done on the high resolution small-angle

Table I. — *Quantities determined from the composition for the two series of samples examined in the system* DDAB/*tetradecane/water.* C_s *is the surfactant concentration,* [W]/[S] *the water-to-surfactant molar ratio,* [O]/[S] *the oil-to-surfactant ratio,* ϕ *the polar volume fraction,* Σ *the calculated interfacial area per unit volume, assuming a headgroup area of* 68 Å^2 *per molecule and* ρ_1 *and* ρ_2 *the electronic densities in the polar and nonpolar regions respectively.*

Sample	D_2O wt %	DDAB wt %	Oil wt %	C_s M	[W]/[S]	[O]/[S]	ϕ %	Σ Å^2/Å^3	ρ_1 eÅ^{-3}	ρ_2 eÅ^{-3}
Tetra 1a	27.0	36.5	36.5	0.73	17.1	2.3	27.9	0.030	0.45	0.27
Tetra 2a	34.0	33.0	33.0	0.67	23.8	2.3	33.7	0.028	0.42	0.27
Tetra 3a	42.0	29.0	29.0	0.60	33.5	2.3	40.6	0.025	0.39	0.27
Tetra 4a	51.0	24.5	24.5	0.52	48.2	2.3	48.7	0.022	0.38	0.27
Tetra 5a	60.0	20.0	20.0	0.43	69.4	2.3	57.2	0.018	0.36	0.27
Tetra 1b	30.0	21.0	49.0	0.40	33.1	5.4	27.1	0.015	0.39	0.27
Tetra 2b	38.0	18.6	43.4	0.37	47.3	5.4	34.0	0.014		0.27
Tetra 3b	46.0	16.2	37.8	0.33	65.7	5.4	41.1	0.013	0.37	0.27

camera D22 at LURE (Orsay, France), and neutron scattering on the same samples (all with D_2O) at the PACE facility at Orphée (Saclay, France). Data reduction was made using standard methods, including absolute scaling by comparison with scattering of pure D_2O [23].

Spectra from along a typical water dilution line are shown in figures 4 and 5. The peak position shifts with water content, D^* increasing with water dilution. A well-defined Porod regime allows an unambiguous determination of Σ. The neutron and X-ray spectra are very similar, hence the assumption of constant bromide counter-ion concentration is valid within the experimental resolution ($q_{max} = 0.5$ Å^{-1}, giving a resolution of 12 Å in real space). This is contrary to the result obtained with SDS systems, in which details of the local electronic densities or scattering length density distributions are responsible for the peak shape and position [48].

We can calculate several quantities of interest from the scattering curves before making reference to any model. The simplest of these is the peak position $D^* = 2\pi/q_{max}$. The experimental value of the specific surface Σ can be deduced from the absolute value in cm^{-5} of the plateau in a Porod plot $q^4 I(q)$ against q. The invariant Q^* is given by

$$Q^* = \int_{q_{min}}^{q_{max}} q^2 I(q)\, dq \tag{7}$$

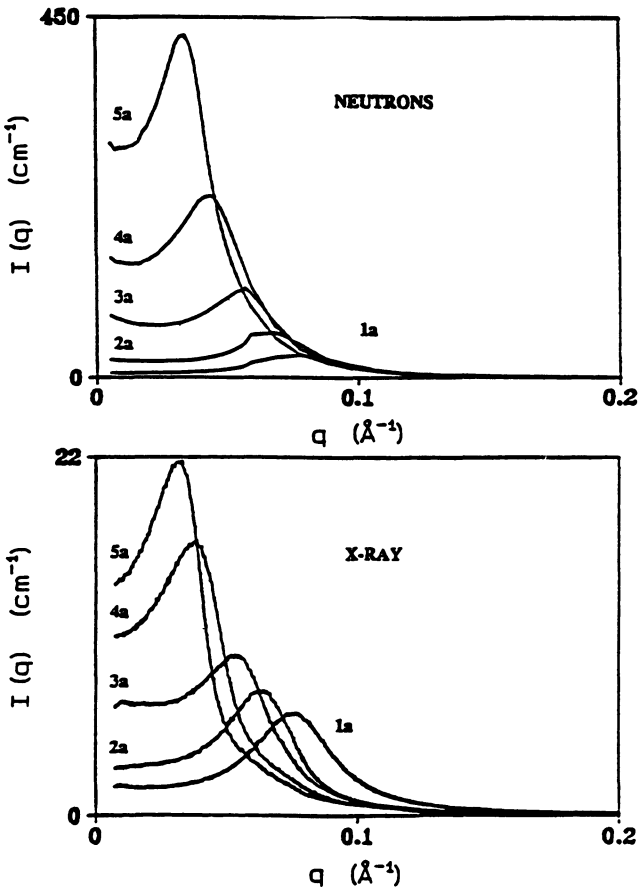

Fig. 4. — Absolute scaled small-angle neutron and X-ray spectra for the samples on dilution line a in the system DDAB/tetradecane/water at 28 °C. Note the extreme similarity between the two sets of spectra.

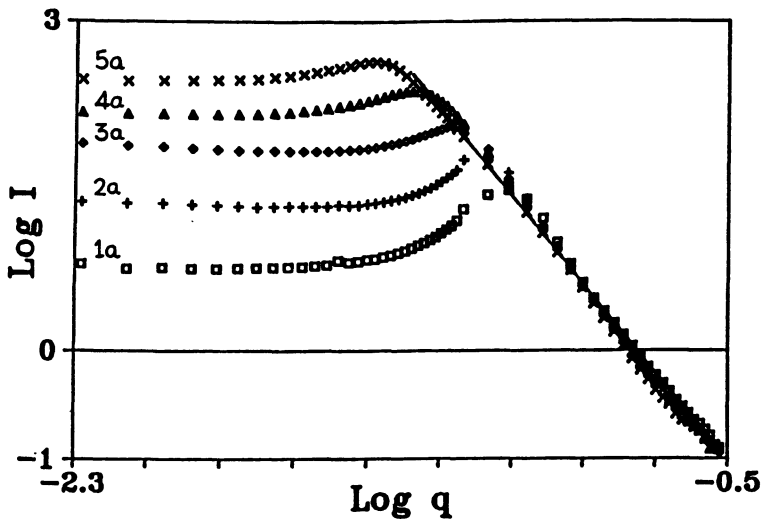

Fig. 5. — Plot of log (I) against log (q) for neutron scattering from the samples along dilution line a in the system DDAB/tetradecane/water. Note the extremely clear Porod law behaviour at large angles.

but can also be calculated from the composition by the expression

$$Q^* = 2\pi^2 \Phi(1 - \Phi)(\rho_1 - \rho_2)^2 . \tag{8}$$

Agreement of these two expressions can be checked, as can the agreement between the values of Σ calculated from the scattering and from the composition. This ensures :

(i) that the two-media assumption — that the sample can be treated as made up of homogeneous polar and nonpolar regions — is justified ;

(ii) that a negligible fraction of the surfactant molecules are molecularly dispersed instead of participating in forming the surfactant film ;

(iii) that the calculated volume fractions and electronic densities are correct ; and

(iv) that the minimum and maximum values of q are correctly chosen.

4. Discussion.

The parameters resulting from fitting a Teubner-Strey expression to the spectra are given in table III, along with values derived from the TPR and (random filling) CRC models. The fits to the Teubner-Strey expression are very good indeed, but as usual one can infer little from these results, in particular nothing about the microstructure. Here we note that ξ is of the same order of magnitude as D^*, which means that a Voronoï lattice is a reasonable choice for structural models. We have also calculated values of the « bicontinuity » parameter C_3 of Chen *et al.* [30] (see Sect. 2.2). While the values vary from over 20 down to 8 we know from conductivity measurements and the fact that the surfactant is insoluble in tetradecane, that the phase is bicontinuous throughout. As a result we are forced to conclude that this criterion is not valid.

The predictions of the other models for the peak position D^* are summarized in tables IV and V. One observes in table II that the measured correlation length ℓ_c is smaller than D^*, the ratio being about 3 for all samples. This is incompatible with the Talmon-Prager, CRC and TPR models, all of which predict $\ell_c \approx D^*$. This is a direct proof of the existence of

Table II. — *Quantities measured from X-ray and neutron scattering experiments for the system* DDAB/*tetradecane/water. D* is the real-space peak position, ℓ_c is the correlation length, Σ is the internal surface and σ the calculated headgroup area per molecule.*

Sample	X-ray				Neutron		
	D^* Å	ℓ_c Å	Σ Å^2/Å^3	σ Å^2	D^* Å	Σ Å^2/Å^3	σ Å^2
Tetra 1a	84	25	0.031	71	80	0.031	71
Tetra 2a	97	31	0.027	67	100	0.029	72
Tetra 3a	120	37	0.029	80	114	0.027	75
Tetra 4a	160	45	0.024	77	150	0.023	74
Tetra 5a	190	53	0.023	89	190	0.019	74
Tetra 1b	157		0.017	71			
Tetra 2b	190		0.015	67			
Tetra 3b	250		0.014	70			

Table III. — *Results of fitting X-ray data for the system* DDAB/*tetradecane/water to the parametric expression of Teubner and Strey and to the Talmon-Prager and cubic random cell models. For the Teubner-Strey expression, d is the spatial periodicity and ξ the correlation distance ; for the other models D* is the real-space peak position and $v/a\ell$ the effective surfactant packing parameter.*

Sample	Teubner-Strey			TPR		CRC	
	d Å	ξ Å	C_3	D^* Å	$v/a\ell$	D^* Å	$v/a\ell$
Tetra 1a	81	52	23	39	1.19	40	1.20
Tetra 2a	93	50	19	46	1.11	48	1.11
Tetra 3a	110	35	8	56	1.04	58	1.05
Tetra 4a	151	52	9	66	0.99	68	1.00
Tetra 5a	177	62	10	79	0.95	82	0.96
Tetra 1b	143	45	8	77	1.11	79	1.11
Tetra 2b	184	60	9	93	1.06	96	1.06
Tetra 3b	235	74	8	108	1.03	112	1.03

local correlations. Full scattering spectra predicted by the water-in-oil spheres and DOC lamellar models are shown compared to the observed scattering in figures 6 and 7. Of these, only the DOC lamellar model appears reasonable.

The peak positions and scattering spectra for the oil-in-water and water-in-oil spherical droplet models were calculated using the Hayter-Penfold RMSA procedure [49], with the droplet charge set to zero. It turns out that the peak positions obtained for a dispersion of water spheres in oil are in reasonable agreement with those measured, even with the radii imposed by the volume fractions and interfacial areas ($R = 3\,\Phi/\Sigma$). The shapes of the scattering curves are not perfect, but are certainly acceptable. However, this model cannot

Table IV. — *Results of attempting to fit data for the system* DDAB/*tetradecane/water with a model of interacting monodisperse spheres. R is the sphere radius, D* the real-space peak position and* $v/a\ell$ *the effective surfactant packing parameter.*

Sample	Oil-in-water			Water-in-oil		
	R Å	*D** Å	$v/a\ell$	*R* Å	*D** Å	$v/a\ell$
Tetra 1a	28	70	1.50	71	130	0.84
Tetra 2a	36	84	1.37	71	130	0.84
Tetra 3a	49	106	1.26	71	140	0.84
Tetra 4a	66	136	1.19	71	140	0.84
Tetra 5a	95	185	1.13	71	150	0.84
Tetra 1b	54	135	1.24	140	260	0.92
Tetra 2b	73	168	1.17	140	260	0.92
Tetra 3b	95	206	1.13	140	262	0.92

Table V. — *Result of attempting to fit data for the system* DDAB/*tetradecane/water with the* DOC *models. For the* DOC *cylinders model (water-filled cylinders in oil), Z is the co-ordination number and r is the cylinder radius. For the* DOC *lamellar model, t is the oil or water half-thickness (the total bilayer thickness is thus* $2t + 2\ell$*) and* ψ *is the pseudo-volume fraction. D* is the real-space peak position and* $v/a\ell$ *the effective surfactant packing parameter.*

Sample	DOC w/o cylinders				DOC reverse lamellae				DOC direct lamellae			
	*D** Å	*Z*	*r* Å	$v/a\ell$	*D** Å	*t* Å	ψ	$v/a\ell$	*D** Å	*t* Å	ψ	$v/a\ell$
Tetra 1a	84	4.5	28	1.34	88	9	0.25	0.98	83	11	0.25	1.03
Tetra 2a	96	4.5	36	1.27	105	12	0.3	0.98	99	11	0.3	1.03
Tetra 3a	118	5	47	1.20	116	16	0.3	0.98	121	11	0.35	1.03
Tetra 4a	143	5	62	1.15	154	22	0.5	0.97	152	11	0.45	1.02
Tetra 5a	184	5	86	1.11	185	31	0.5	0.97	191	11	0.5	1.01
Tetra 1b	156	3.5	55	1.19	176	18	0.25	0.99	166	34	0.25	1.02
Tetra 2b	190	4	71	1.14	188	24	0.25	0.99	198	33	0.3	1.02
Tetra 3b	229	5	91	1.11	254	31	0.4	0.99	253	31	0.45	1.02

explain the high conductivity of the L_x phase. It also requires an *ad hoc* variation of the surfactant parameter $v/a\ell$ from 1.13 to 1.5 with composition, which we regard as unlikely. Oil-in-water droplets give systematically wrong peak positions in the scattering.

Dismissal of the DOC-cylinder model is more difficult. This structure would explain the conductivity of the L_x phase, but not the nature of the phase transitions and equilibria. In the adjacent cubic phase and in both the lamellar phases the surfactant forms a bilayer and not a monolayer. Furthermore, the scattering can only be reconciled with a connected cylinder structure if one assumes an unlikely variation of the surfactant parameter. The proposed structure has a connectivity *Z* of about 5 throughout the stability range of the L_x phase. While

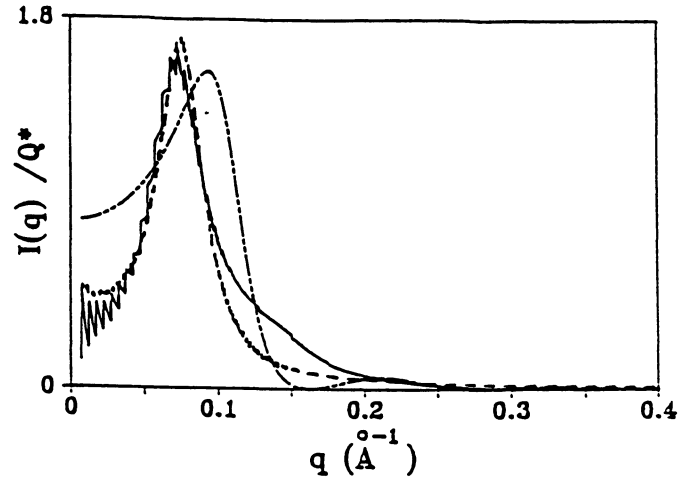

Fig. 6. — Comparison between measured and calculated spectra for sample 1a. The full curve is the normalised X-ray scattering data, the dashed-dotted curve is the prediction of water spheres in oil and the dashed curve that of the DOC reversed lamellar model.

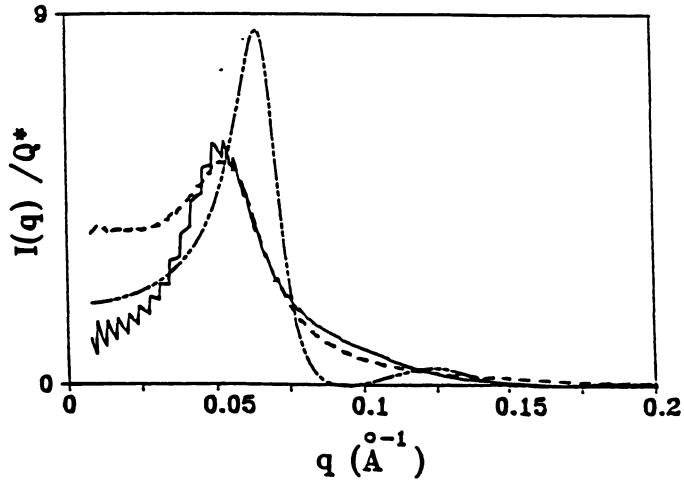

Fig. 7. — Comparison between measured and calculated spectra for sample 3a. Curves are labelled as for figure 6.

this would certainly give the high conductivities observed, the packing constraint would have to be relaxed and $v/a\ell$ allowed to vary by over 20 % for this to work. The DOC-cylinder structure must therefore be rejected, even though it is compatible with the peak position.

This leaves the DOC lamellar model. This structure has already been found in other systems and is referred to as the L_3 or « sponge » phase by other authors. Since the L_x phase is in the middle of the ternary phase diagram, the DOC-lamellar structure could be *a priori* a reversed (water inside the bilayer) or a direct bilayer (oil inside). The calculations in table V show that either structure is plausible. Both give reasonably good prediction of the peak position along with $v/a\ell$ close to 1 and fairly constant. This is to be expected from

Babinet's principle : an exchange of polar and nonpolar regions does not change the scattering.

However, since the neighbouring cubic phase is a reversed bilayer structure, we conclude that the L_x phase should also be, in order to explain the extremely temperature-sensitive phase transition between them. This structure would also explain why the phase cannot be diluted with water or oil, since unfolding or excessive swelling of this random lamellar structure would induce forbidden variations of $v/a\ell$.

While it is always possible to calculate the full scattering curve using the cube method [8], setting up the array of cubes is extremely cumbersome for Voronoï models like this. Instead we obtain a fairly good approximation to the full scattering curve $I(q)$ by multiplying the $S(q)$ of the underlying lattice by the $P(q)$ of the average polygonal face. The excluded volume is determined by assuming that if the distribution of centres is too random, then there will be places at which the bilayer is forced to bend too sharply. Excluding such configurations is achieved by imposing a minimum distance of approach of the order of $\frac{1}{2} n^{-\frac{1}{3}}$. This gives an excluded volume of approximately 50 %. This causes the distribution of the centres to be quite regular.

The form factor is obtained by approximating the polygonal faces by disks of thickness $2\,t$ for the reversed bilayer (or $2(\ell + t)$ for the normal bilayer) and radius one quarter the nearest neighbour distance. (This gives roughly the correct surface area for the cells.) This procedure neglects correlations between adjacent facets — in particular the fact that the facet-facet correlation function will certainly be anisotropic — but is otherwise reasonably sound. It has been checked against optical Fourier transforms of two-dimensional realisations of the DOC-lamellar model [34] and found to give fair agreement.

It is possible to deduce the geometric limits on the random lamellar structure from the positions of the phase boundaries (see Fig. 8). This is somewhat similar to the phase boundary

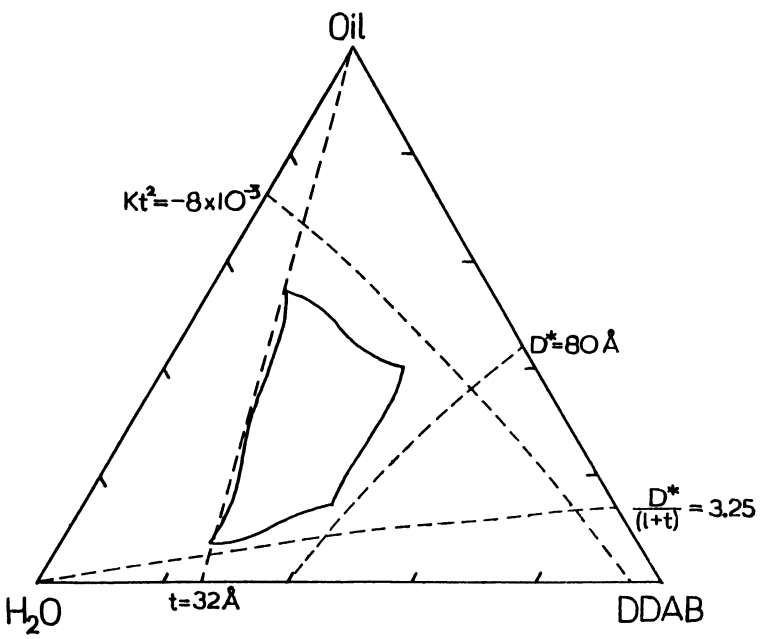

Fig. 8. — Measured boundaries of the L_x single-phase region compared with the limits imposed by various geometric constraints on the proposed DOC-lamellar microstructure.

calculation made for the DOC-cylinder model [7]. The left-hand phase boundary lies essentially along a line of constant surfactant/water ratio. This is equivalent to an upper limit on the water film thickness, which is never more than about 64 Å. Beyond this limit it seems that the structure is no longer stable and the dilute lamellar phase, with water thickness at least 70 Å is in excess.

The right edge is approximately an upper limit on the surfactant concentration. This is directly linked to the cell size, and thus to the peak position D^*. Once D^* is less than about 80 Å (Fig. 8) the phase prefers to go into equilibrium with the concentrated lamellar phase, which has hydrocarbon thickness about 27 Å, slightly less than two fully-extended chain lengths. Larché [14] has noted that this equilibrium is extremely temperature-sensitive. This could be one of the first examples of an unbinding transition between highly charged concentrated bilayers [50].

The top and bottom boundaries of this phase appear to be set by limits on the allowed curvature of the reverse bilayer. Dilution with oil has the effect of trying to flatten out the bilayer, which has negative Gaussian curvature. The limit appears to be roughly $\langle K \rangle \; t^2 \approx 10^{-2}$: in other words the principal curvature radii cannot be greater than about five times the total water thickness. A first effect of this appears to be a breaking of the symmetry between the two sides of the bilayer. While making ψ different to $\frac{1}{2}$ at constant cell size changes the curvature in the wrong direction, at constant composition it has the compensatory effect of reducing the cell size and in fact keeps $\langle K \rangle$ negative maintaining the desired degree of « foldedness ». The limit is reached when ψ approaches 0.18, at which point $\langle K \rangle$ must change sign and no amount of change in the cell size will keep the surface sufficiently folded (see Fig. 3). Approximate phase boundaries deduced from geometric constraints on the DOC lamellar structure are shown compared to the experimental phase boundaries in figure 8.

Our model calculations give values of the pseudo-volume fraction ψ ranging between 0.25 and 0.5. This gives a bicontinuous structure, in agreement with the conductivity measurements, with a mean curvature which is not too far from zero. The total bilayer thickness $(2\,t + 2\,\ell)$ is generally of the order of $D^*/2$. The persistence length, the typical distance over which the bilayer normal remains roughly parallel to itself is also about $D^*/2$, as for all Voronoï models.

This model also gives some understanding of the slow increase of conductivity with water content. Along any water dilution line the bilayer thickness increases. The connectivity of the bilayer also increases as ψ relaxes to its desired value of $\frac{1}{2}$.

5. Conclusion.

In the DDAB/tetradecane/water system all the standard models run into problems when tested against the scattering data. The cubic random cell model and both variants of the Talmon-Prager model predict the peak in the wrong position unless local correlations are introduced. Droplets or DOC cylinder models require unlikely *ad hoc* variation of the surfactant parameter $v/a\ell$ with water content and cannot be reconciled with the phase diagram. Of the quantitative models, only the DOC-lamellar model, describing a random bilayer, is compatible with the observed scattering. We therefore conclude that the observed microemulsion region is a DOC-lamellar (or L_3) phase. This model is compatible not only with the scattering data but also with the conductivity measurements and the experimental phase diagram. It gives a simple explanation for the positions of the measured phase boundaries in terms of such geometric constraints on the structure as the bilayer thickness, the cell size and the film curvature.

At high water contents it may appear strange to be proposing a « reversed » structure for this phase. It should be noted however that in this structure the curvature is not towards the water ; in fact $v/a\ell$ is slightly less than one, indicating curvature of the surfactant monolayers towards the oil. Also, even for sample 5a, at the water-rich corner of the single-phase region, the total water thickness proposed is only 60 Å out of a total cell size of 180 Å. While this certainly means we are not in the regime of validity of thin-plate theory, the reversed bilayer description still makes sense.

For surfactant systems with lower bending constant k_c, this structure is restricted to a very narrow channel near the edge of the lamellar phase. In this system it extends over a much broader range of composition, but still has in common with other L_3 phases the ability to be in equilibrium with excess oil and lamellar phase. This is not the first example of a more concentrated L_3 structure : such a phase was mapped out by Ekwall in the central region of the ternary sodium octanoate/octanoic acid/water system [51]. In that system, as in this one, the disordered lamellar structure exhibits a peak in scattering. In diluted L_3 structures on the other hand, where no spontaneous curvature restricts the swelling [20, 52], the scattering can be divided into a low-q part where $I(q)$ is approximately constant, followed at $q > 2\pi/D^*$, by a region in which $I(q) \sim q^{-2}$, and finally a Porod region where $I(q) \sim q^{-4}$. In the case studied here, the scattering is dominated by the interaction peak which merges into the Porod limit at high q.

Closely related to the DOC lamellar model is the molten cubic structure. This is also a random bilayer, the main difference being that it always has zero mean curvature, even if the pseudo-volume fractions on the two sides are different, but does not offer the continuous transition to disconnected vesicles built into the DOC lamellar model. Without more knowledge of such structures this remains speculative ; perhaps the symmetry breaking predicted here upon oil dilution means that the « molten cubic » model would have to include similar features in order to work.

Acknowledgments.

We thank Francis Larché for letting us use his phase diagram, Loic Auvray at Orphée and Claudine Williams at LURE for their assistance with the scattering measurements, Didier Roux and H. S. Chen for access to preprints before publication, Reinhard Strey for experimental hints on making phase diagrams and communication of his model calculation programs and Stjepan Marcelja for extremely valuable discussions.

This work was made possible by the program of Franco-Australian scientific collaboration instituted by Professor Michel Ronis of the French Embassy in Canberra. This program enabled three of us to make extended visits to foreign laboratories.

Appendix 1.

Curvature of facetted surfaces.

Consider a surface made up of flat pieces joined along straight lines. The mean curvature H and the Gaussian curvature K are both zero wherever they exist — that is everywhere except at the edges and vertices, where they are undefined. Nonetheless, the integrated curvatures

$$\mathcal{H} = \int_S H \, dA \tag{9}$$

and

$$\mathcal{K} = \int_S K \, dA \tag{10}$$

are not in general equal to zero, and neither are the area-averaged curvatures

$$\langle H \rangle = \frac{\mathcal{H}}{A} \tag{11}$$

and

$$\langle K \rangle = \frac{\mathcal{K}}{A} . \tag{12}$$

All the curvature is concentrated at the edges and vertices. To proceed, we consider edges and vertices as the zero-radius limits of suitable pieces of cylinders, spheres or other surfaces, and thus calculate the correct contributions to $\mathcal{H}$ and $\mathcal{K}$ [53].

First consider an edge of length L and dihedral angle α. This must always be measured on the same side of the surface and will therefore be greater than or less than π according as the bend is towards or away from the chosen side. We choose our normal vector to point in the direction of this chosen side, so that if the curvature is towards this side it will be counted as positive. Thus we expect that if $\alpha < \pi$ then the contribution to $\mathcal{H}$ will be positive and if $\alpha > \pi$ then it will be negative. Let us now remove narrow strips from along each side of this edge and replace them by a piece of cylinder of radius r which joins smoothly to the remaining flat pieces. In order for this to happen, this piece must subtend an angle of $|\pi - \alpha|$ and have length L (plus a small correction of order r which takes account of what happens at the ends). At every point of this piece, the mean curvature is $1/2r$ if $\alpha < \pi$ and $-1/2r$ if $\alpha > \pi$. As for any cylinder, the Gaussian curvature is zero. So the surface integral of the Gaussian curvature is zero and that of the mean curvature is

$$(\pi - \alpha)(L + \varepsilon r)/2 . \tag{13}$$

Notice that the sign is always correct here : the absolute value and the change of sign in the curvature have cancelled. Taking the limit as $r \to 0$ gives the mean curvature contribution for a single edge

$$\mathcal{H} = (\pi - \alpha) L/2 . \tag{14}$$

The situation at a vertex is similar. Suppose that n faces meet at a point and that the face angles are β_i. If $\sum \beta_i < 2\pi$ then this vertex may be replaced by a spherical polygon with radius r, n sides and vertex angles $\pi - \beta_i$. As this has area

$$\begin{aligned} A &= \left(\sum_{i=1}^{n} (\pi - \beta_i) - (2 - n)\pi \right) r^2 \\ &= \left(2\pi - \sum \beta_i \right) r^2 \end{aligned} \tag{15}$$

and the mean and Gaussian curvatures at every point are $1/r$ and $1/r^2$ respectively, the integrated mean curvature is $\left(2\pi - \sum \beta_i\right) r$ and the integrated Gaussian curvature is $2\pi - \sum \beta_i$. Letting $r \to 0$ as before, we see that the vertex contributes nothing to $\mathcal{H}$, and $2\pi - \sum \beta_i$ to $\mathcal{K}$.

If $\sum \beta_i > 2\pi$ then a piece of a sphere will not do ; something saddle-shaped is needed. But clearly the mean curvature is always going to be zero : no matter what the details, the area must be proportional to r^2 while H goes like $1/r$. For the Gaussian curvature, the correct approach is to use the Gauss map, which sends every point on the surface to that point on the

unit sphere corresponding to the direction of the normal vector. The area of the image of a region under this map is its integrated Gaussian curvature, with the proviso that the area should be counted as negative if the vertex order is reversed by the mapping. Careful application of this method gives the required result : regardless of whether the vertex angles sum to less or more than 2π, the Gaussian curvature contribution of a vertex is

$$\mathcal{K} = 2\pi - \sum \beta_i \,. \tag{16}$$

So for any surface built up in this way, the total curvatures $\mathcal{H}$ and $\mathcal{K}$ are simply obtained by summing these contributions over all edges and vertices respectively. Dividing by the total surface area then gives the area-averaged curvatures.

Appendix 2.

Packing on curved surfaces.

In order to relate the surfactant packing parameter $v/a\ell$ for various models to the area-averaged curvatures, we recall that for a small element of surface,

$$A(x) = A(0)(1 + 2Hx + Kx^2) \tag{17}$$

where $A(0) = A$ is the area of the original surface and $A(x)$ is the area of the parallel surface displaced a distance x in the direction of the normal vector [54]. We now consider three different decorations to our facetted surface :

(i) a surfactant monolayer with the tails of length ℓ on the « negative » side of the surface (see Fig. 9a) ;

(ii) a normal oil-swollen bilayer with oil half-thickness t and surfactant tails of length ℓ, so that the total bilayer thickness is $2\ell + 2t$ (see Fig. 9b) ; and

(iii) a reverse bilayer with water half-thickness t and again tails of length ℓ (see Fig. 9c).

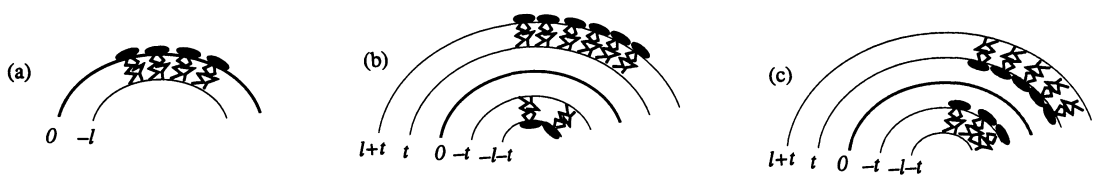

Fig. 9. — The three ways to decorate a surface with a surfactant film : (a) a monolayer, (b) a normal (oil-swollen) bilayer, and (c) a reversed bilayer. The original surface is labelled 0, parallel surfaces are labelled by the distance they are displaced in the direction of the normal vector.

For the monolayer the total volume occupied by the tails is

$$\begin{aligned} v &= \int_{-\ell}^{0} A(x)\,\mathrm{d}x \\ &= A(0)\,\ell\left(1 - \langle H\rangle\,\ell + \frac{1}{3}\langle K\rangle\,\ell^2\right) \end{aligned} \tag{18}$$

and as the total headgroup area is just $A(0)$, the average value of the surfactant parameter is

$$v/a\ell = 1 - \langle H\rangle\,\ell + \frac{1}{3}\langle K\rangle\,\ell^2 \,. \tag{19}$$

For the normal oil-swollen bilayer, the tail volume is

$$v = \int_{-\ell-t}^{-t} A(x)\,\mathrm{d}x + \int_{\ell}^{\ell+t} A(x)\,\mathrm{d}x$$
$$= 2A(0)\,\ell\left(1 + \langle K\rangle\left(t^2 + \ell t + \frac{1}{3}\ell^2\right)\right) \tag{20}$$

and the total headgroup area is

$$a = A(-\ell - t) + A(\ell + t)$$
$$= 2A(0)(1 + \langle K\rangle(\ell + t)^2) \tag{21}$$

so that

$$v/a\ell = 1 - \left(\ell t + \frac{2}{3}\ell^2\right)\frac{\langle K\rangle}{1 + \langle K\rangle(\ell + t)^2}\,. \tag{22}$$

In the limit of no swelling this reduces to

$$v/a\ell = 1 - \frac{2\langle K\rangle\,\ell^2}{3(1 + \langle K\rangle\,\ell^2)}\,. \tag{23}$$

For a reversed bilayer the total tail volume is the same as for the normal bilayer, but the headgroup area is

$$a = A(-t) + A(t)$$
$$= 2A(0)(1 + \langle K\rangle\,t^2) \tag{24}$$

and so

$$v/a\ell = 1 + \left(\ell t + \frac{1}{3}\ell^2\right)\frac{\langle K\rangle}{1 + \langle K\rangle\,t^2}\,. \tag{25}$$

Appendix 3.

Voronoï statistics.

We consider models in which the facetted surface is constructed as described in the text by random filling of a Voronoï tesselation of density n with A and B in the fractions ψ and $1 - \psi$, and the selection of those faces which separate differently filled cells. This general framework, combined with decoration (i) above is the Talmon-Prager model ; combined with (ii) or (iii) it gives a direct or reverse disordered infinite folded bilayer phase : the DOC lamellar models (see Fig. 2).

For this analysis, we are forced to avoid any condition of closest approach — this is « true » not « hard sphere » Voronoï — even though that is what really interests us. So the results of this section are only strictly valid for the original Talmon-Prager model, which uses the true Voronoï lattice. For the « repulsive » version of the Talmon-Prager model and for the DOC lamellar model, the results are only correct in the limit of small n. For moderate cell densities we assume that this approximation is no worse than any of the others made in these models.

Statistics for the full Voronoï lattice have been calculated by Meijering [55]. The average number of vertices per cell is approximately 27.07, so as each vertex is at the common point of four cells, the total number of vertices per unit volume is $27.07\,n/4$. The average total edge length per unit volume is $5.83\,n^{2/3}$ and the total surface area per unit volume is $2.91\,n^{1/3}$.

To calculate the average curvatures, we first have to know the total surface by which to divide. Now a face is « real » if it separates cells of different type, that is, with probability $2\psi(1-\psi)$. So the « real » surface area per unit volume is

$$A/V = 2(2.91)\,\psi(1-\psi)\,n^{1/3}. \tag{26}$$

From Appendix 1,

$$\mathcal{K} \sum_{\text{edges}} (\pi - \alpha)\,L/2 \tag{27}$$

and so as α and L are independent random variables

$$\mathcal{K}/V = \frac{1}{2}\,\langle \pi - \alpha \rangle\,(L_{\text{tot}}/V) \tag{28}$$

where L_{tot} is the total edge length per unit volume. There are four possible edge configurations : AAA, AAB, ABB and BBB. The first and last contribute nothing : there is no « real » edge. If we adopt the convention that dihedral angles are measured on the A side of the surface (so that $H > 0$ corresponds to curvature towards medium A), then as the dihedral angles are $2\pi/3$ on average, AAB has $\langle \alpha \rangle = 4\pi/3$, and ABB has $\langle \alpha \rangle = 2\pi/3$. So

$$\begin{aligned}\langle \pi - \alpha \rangle &= 3\,\psi^2(1-\psi)\,\frac{-\pi}{3} + 3\,\psi(1-\psi)^2\,\frac{+\pi}{3} \\ &= \pi\psi(1-\psi)(1-2\psi)\end{aligned} \tag{29}$$

whence

$$\langle H \rangle \approx (1.57)\,n^{1/3}\,(1-2\psi). \tag{30}$$

Note that this is zero only when $\psi = \frac{1}{2}$.

We proceed similarly for vertices. According to Winterfield [56], the expected angle between two adjacent edges in the Voronoï tesselation is approximately

$$\langle \beta_i \rangle = \beta \simeq 1.93966 \text{ radians} \approx 111°\,8' \tag{31}$$

which is slightly larger than the tetrahedral coordination angle of approximately 109° 28'. There are five possible vertex configurations, of which again the all-A and all-B contribute nothing. For the configurations AAAB and ABBB, which occur with probabilities $4\psi^3(1-\psi)$ and $4\psi(1-\psi)^3$ respectively, we expect $2\pi - \sum \beta_i = 2\pi - 3\beta$, while for AABB, which occurs with probability $6\psi^2(1-\psi)^2$ it is $2\pi - 4\beta$. So

$$\begin{aligned}\mathcal{K}/V &= \frac{27.07\,n}{4}\left\langle 2\pi - \sum \beta_i \right\rangle \\ &= \frac{27.07\,n}{4}\,\psi(1-\psi)((4\psi^2 - 4\psi + 8)\,\pi - 12\,\beta)\end{aligned} \tag{32}$$

and therefore

$$\begin{aligned}\langle K \rangle &= \frac{(27.07)}{(8 \times 2.91)}\,n^{2/3}((1-2\psi)^2\,\pi + 7\,\pi - 12\,\beta) \\ &\approx ((3.65)(1-2\psi)^2 - (1.49))\,n^{2/3}.\end{aligned} \tag{33}$$

This is negative for $0.18 < \psi < 0.82$. The packing parameter $v/a\ell$ can be derived immediately from this result and those of Appendix 2.

Appendix 4.

Parameter values.

The relations derived in Appendices 2 and 3 can be used to determine values for the model parameters from the composition of a sample. For the Talmon-Prager model (repulsive or not, although the values derived from Voronoï statistics will not be exact for the repulsive version) we have the following simple relations :

$$\begin{aligned} \psi &= \Phi \\ n^{1/3} &= \frac{\Sigma}{(5.82)\,\psi(1-\psi)} \end{aligned} \tag{34}$$

and from Appendices 2 and 3,

$$\begin{aligned} \langle H \rangle &= (1.57)\, n^{1/3}(1-2\psi) \\ \langle K \rangle &= ((3.65)(1-2\psi)^2 - (1.49))\, n^{2/3} \end{aligned} \tag{35}$$

and finally

$$v/a\ell = 1 - \langle H \rangle\, \ell + \frac{1}{3}\langle K \rangle\, \ell^2 . \tag{36}$$

That is, the values of Φ and Σ determine the parameters ψ and n. This model does not have enough parameters to allow fitting to the surfactant parameter $v/a\ell$ as well.

For the reverse bilayer, that is, a water film of thickness $2\,t$ separating bulk oil regions, we require simultaneous solution of

$$\begin{aligned} \Phi &= (11.64)\, n^{1/3} t\psi(1-\psi)\left(1 + \frac{1}{3}\langle K \rangle\, t^2\right) \\ \Sigma &= (11.64)\, n^{1/3}\psi(1-\psi)(1 + \langle K \rangle\, t^2) \end{aligned} \tag{37}$$

where the Gaussian curvature is given by

$$\langle K \rangle = ((3.65)(1-2\psi)^2 - (1.49))\, n^{2/3} \tag{38}$$

and ψ is chosen to give the correct value for the surfactant packing parameter

$$v/a\ell = 1 + \left(\ell t + \frac{1}{3}\ell^2\right)\frac{\langle K \rangle}{1 + \langle K \rangle\, t^2} . \tag{39}$$

So these three relations for the known quantities Φ, Σ and $v/a\ell$ determine the values of the model parameters ψ, n and t.

Finally, for the oil-swollen normal bilayer we need solutions of

$$\begin{aligned} \Phi &= (11.64)\, n^{1/3}(\ell + t)\,\psi(1-\psi)\left(1 + \frac{1}{3}\langle K \rangle\,(\ell + t)^2\right) \\ \Sigma &= (11.64)\, n^{1/3}\psi(1-\psi)(1 + \langle K \rangle\,(\ell + t)^2) \end{aligned} \tag{40}$$

with curvature as for the reversed bilayer, but with $v/a\ell$ given by

$$v/a\ell = 1 - \left(\ell t + \frac{2}{3}\ell^2\right)\frac{\langle K \rangle}{1 + \langle K \rangle\,(\ell + t)^2} . \tag{41}$$

Again these three constraints determine the values of the three model parameters.

Appendix 5.

Approximate phase boundaries.

For any composition whatsoever, the equations of Appendix 4 can be solved to give values for the cell density n, film thickness t and pseudo-volume fraction ψ for either of the DOC lamellar models. At some points these values will be totally unrealistic and the structure obtained could not be adopted by a real surfactant film. By performing this calculation at regularly spaced points throughout the phase diagram and marking those at which various physically reasonable constraints on the structure are satisfied, we can gain some insight into the behaviour of this model.

Figure 8 is the result of such calculations on the model of reverse lamellae. The first observation was that the surfactant parameter $v/a\ell$ is a very slowly varying function of the other variables, so that fitting to it would be numerically unstable. Simply setting $\psi = \frac{1}{2}$ and fitting n and t to the calculated Φ and Σ at each point in the phase diagram leads to values of $v/a\ell$ which vary between about 0.95 and 0.99, not beyond the bounds of possibility. The structures produced with this simplification fit the scattering at high water content but not towards the top of the single-phase region : there they have values of D^* which are too high.

It is this observation which leads to the counterintuitive behaviour of the curvature with respect to ψ which is mentioned in the text. In order to obtain the peak position found in the experiment, one has to change ψ. This reduces the cell size very rapidly, resulting in the film becoming *more* rather than less folded overall (more precisely, its Gaussian curvature gets more negative) : it has less « folds » per cell, but many more cells per unit volume. Such a pattern continues only so long as the « number of folds per unit volume » remains positive, that is while ψ is larger than about 0.18. After this, the Gaussian curvature changes sign.

Postulating that a minimum or maximum water thickness might be one of the determining constraints leads to the observation that lines of constant thickness are approximately lines of constant water to surfactant ratio. This is easily seen in the equations, at least to first order. Similarly, the cell size is a function of surfactant content only, and the curvature of the film, when normalized by the thickness, depends very roughly on the oil to water ratio.

References

[1] NINHAM B. W., BARNES I. S., HYDE S. T., DERIAN P.-J. and ZEMB T. N., *Europhys. Lett.* **4** (1987) 561.

[2] WARR G. G., ZEMB T. N. and BARNES I. S., Proceedings of the World Surfactants Congress (CESIO editor, Paris) 1988.

[3] ZEMB T. N., HYDE S. T., DERIAN P.-J., BARNES I. S., NINHAM B. W., *J. Phys. Chem.* **91** (1987) 3814.

[4] BARNES I. S., HYDE S. T., NINHAM B. W., DERIAN P.-J., DRIFFORD M., WARR G. G., ZEMB T. N., *Progr. Coll. Polym. Sci.* **76** (1988) 90.

[5] BARNES I. S., HYDE S. T., NINHAM B. W., DERIAN P.-J., DRIFFORD M., ZEMB T. N., *J. Phys. Chem.* **92** (1988) 2286.

[6] ISRAELACHVILI J. N., MITCHELL D. J. and NINHAM B. W., *J. Chem. Soc. Faraday Trans. II* **72** (1976) 1525.

[7] HYDE S. T., NINHAM B. W., ZEMB T. N., *J. Phys. Chem.* **93** (1989) 1464.

[8] BARNES I. S., ZEMB T. N., *J. Appl. Cryst.* **21** (1988) 373.

[9] ZEMB T. N., BARNES I. S., DERIAN P.-J., NINHAM B. W., *Prog. Coll. Polym. Sci.* **81** (1990) 20.

[10] EVANS D. F., MITCHELL D. J., NINHAM B. W., *J. Phys. Chem.* **87** (1983) 538.

[11] EVANS D. F., MITCHELL D. J., NINHAM B. W., *J. Phys. Chem.* **89** (1984) 711.
[12] EVANS D. F., MITCHELL D. J., NINHAM B. W., *J. Phys. Chem.* **90** (1986) 2817.
[13] CHEN S. J., EVANS D. F., NINHAM B. W., *J. Phys. Chem.* **88** (1984) 1631.
[14] LARCHÉ F., unpublished data.
[15] KAHLWEIT M., STREY R., FIRMAN P., HAASE D., JEN J., SCHMACKER R., *Langmuir* **4** (1988) 499.
[16] HYDE S. T., *J. Phys. Chem.* **93** (1989) 1458.
[17] BAROIS P., HYDE S. T., NINHAM B. W., DOWLING T., *Langmuir* **6** (1990) 1136.
[18] RADLINSKA E. Z., HYDE S. T., NINHAM B. W., *Langmuir* **5** (1989) 1427.
[19] CATES M. E., ROUX D., ANDELMANN D., MILNER S. T., SAFRAN S. A., *Europhys. Lett.* **5** (1988) 733.
[20] PORTE G., APPELL J., BASSEREAU P., MARIGNAN J., *J. Phys. France* **50** (1989) 1335.
[21] HAYTER J. B., PENFOLD J., Physics of Complex and Supermolecular Fluids, Eds. S. A. Safran, N. A. Clark (1985) p. 21.
[22] SHARMA R. V., SHARMA K. C., *Physica* **89A** (1977) 213.
[23] ZEMB T. N., French CEA Report R-5301 (1985).
[24] KALER E. W., DAVIS H. T., SCRIVEN L. E., *J. Chem. Phys.* **79** (1983) 5685.
[25] SAMSETH J., CHEN S. H., LITSTER J. D., *J. Appl. Cryst.* **21** (1988) 835.
[26] SINGH H. N., SHANTI S., SINGH R. P., DALEEM S. M., *Ber. Bunsenges. Phys. Chem.* **87** (1983) 1115-1120.
[27] RUSHFORTH D. S., SANCHEZ-RUBIO M., SANTOS-VIDALS L. M., WORMUTH K. R., KALER E. W., CUEVAS R. and PUIG J. E., *J. Phys. Chem.* **90** (1986) 6668.
[28] PUIG J. E., RODRIGUEZ-SIORDIA I., RANGEL-ZAMUDIO L. I., BILLMAN J. F., KALER E. W., *Langmuir* **4** (1988) 806.
[29] TEUBNER M., STREY R., *J. Chem. Phys.* **87** (1987) 3195.
[30] CHEN S. H., CHANG S. L., STREY R., *Prog. Coll. Polym. Sci.* (in press).
[31] VONK C. G., BILLMAN J. F., KALER E. W., *J. Chem. Phys.* **88** (1988) 3970.
[32] BERK N. F., *Phys. Rev. Lett.* **58** (1987) 2718.
[33] CAHN J. W., *J. Chem. Phys.* **42** (1965) 93.
[34] WELBERRY T. R., ZEMB T. N., *J. Colloid. Interf. Sci.* **123** (1988) 413.
[35] MARCELJA S. T., preprint.
[36] TALMON Y., PRAGER S., *J. Chem. Phys.* **76** (1982) 1535.
[37] KALER E. W., PRAGER S., *J. Colloid and Interface Sci.* **86** (1982) 359.
[38] ABILLON O., BINKS B. P., OTERO C., LANGEVIN D., OBER R., *J. Phys. Chem.* **92** (1988) 4411.
[39] DEGIORGIO V., CORTI M., *Chem. Phys. Lett.* **151** (1988) 349.
[40] ANDELMAN D., CATES M., ROUX D., SAFRAN S. A., *J. Chem. Phys.* **87** (1987) 7229.
[41] SAFRAN S. A., ROUX D., CATES M., ANDELMAN D., *Phys. Rev. Lett.* **57** (1986) 491.
[42] JOUFFROY J., LEVINSON P., DE GENNES P. G., *J. Phys. France* **43** (1982) 1241.
[43] AUVRAY L., COTTON J.-P., OBER R., TAUPIN C., Physics of Complex and Supermolecular Fluids, Eds. S. A. Safran, N. A. Clark (1985) p. 449.
[44] MILNER S. T., SAFRAN S. A., ANDELMAN D., CATES M. E. and ROUX D., *J. Phys. France* **49** (1988) 1065.
[45] SCRIVEN L. E., Micellization, Solubilisation and Microemulsions, Ed. K. L. Mittal, Volume 2 (1977) p. 877.
[46] PORTE G., GOMATI R., EL HAITAMY O., APPELL J., *J. Phys. Chem.* **90** (1986) 5746.
[47] HELFRICH W. F., *Z. Naturforsch.* **28C** (1973) 693.
[48] ZEMB T. N., CHARPIN P., *J. Phys. France* **46** (1985) 249.
[49] HANSEN J. P., HAYTER J. B., *Mol. Phys.* **46** (1982) 651.
[50] WENNERSTRÖM H., *Langmuir* (in press).
[51] EKWALL P., *Colloid and Polym. Sci.* **267** (1989) 607.
[52] GAZEAU D., BELLOCQ A. M., ROUX D., ZEMB T. N., *Europhys. Lett.* **9** (1989) 447.
[53] DERIAN P.-J., Ph. D. Thesis, University Paris VI (1989).
[54] GOETZ A., Introduction to Differential Geometry, Addison-Wesley : Reading (1970) p. 268.
[55] MEIJERING J. L., *Philips Res. Rep.* **8** (1953) 270.
[56] WINTERFIELD P., Ph. D. Thesis, University of Minnesota (1981).